Wiley Analytical Science

The Current State of Reconstruction Technologies for 3D X-ray Microscopy including Algorithmic Innovation for AI-based Recovery

April 26, 10:00am - 11:00am EDT

Many properties can only be fully understood in 3D, such as porosity and tortuosity in porous materials, network connection maps in neuroscience, or mechanical properties in 3D additively manufactured structures. X-ray microscopy provides a unique method to image samples non-destructively in 3D across a wide range of materials and life sciences.

Watch this session during the WAS Virtual Conference:

Nicolas Guenichault, Ph.D.

Dr. Stephen T. Kelly, Ph.D.

Register Now

This talk is sponsored by ZEISS

ADVANCED OPTICAL MATERIALS
www.advopticalmat.de

Laser-Printed Terahertz Plasmonic Phase-Change Metasurfaces

Ying Zeng, Dunzhu Lu, Xingxing Xu, Xiaoqiuyan Zhang, Hujie Wan, Junqin Wang, Xuju Jiang, Xiaosheng Yang, Ming Xu, Qiye Wen, Jianquan Yao, Min Hu,* Xinliang Zhang, and Peining Li**

Chalcogenide phase-change materials (PCMs) have offered an appealing material solution by acting as a switchable dielectric layer to tune the electromagnetic properties of terahertz metamaterials and metasurfaces. Here, this work demonstrates large-scale and lithography-free manufacturing of all-PCM terahertz metasurfaces based on direct laser switching of crystalline microdomains in a thin film with high switching ratio of the emerging plasmonic PCM, In_3SbTe_2 (IST). The fabricated high-quality IST metasurfaces achieve efficient plasmonic resonances and a large modulation depth with ultrafast response (full width at half maxima of the modulation time ≈1.6 ps) in a deep-subwavelength switching volume. For the dynamic evolution of terahertz resonance modes, theoretical modeling reveals a delicate interplay between amorphous and crystalline IST due to the bonding-structure-induced different carrier lifetimes and spatially localized electric fields. These studies open new avenues for realizing all-PCM terahertz ultrafast nanophotonics.

1. Introduction

The rapid development of terahertz (THz) technology provides exciting opportunities for vast applications ranging from security screening, spectroscopy, remote sensing, to sixth-generation wireless communications.[1–3] Among various emerging technologies, plasmonic metasurfaces can confine, guide and manipulate THz waves in deep-subwavelength scale which is superior to dielectric metasurfaces for the realization of THz nanophotonics.[4–11] A further step toward tunable THz metasurfaces is offered by chalcogenide phase-change materials (PCMs).[12–15] They can be thermally,[16–18] electrically, or optically[19–21] switched between the amorphous and crystalline states without static power consumption after the removal of external stimulus, leading to the non-volatilely switched strong THz optical contrast and enabling convenient programming. Yet, efforts of PCM-based terahertz metasurfaces with effective plasmonic resonances reported so far rely on layers or patches of PCMs that reside with metallic microstructures.[22–29] Challenges remain that the low conductivity and high ohmic loss of the crystalline PCM may lead to an over-damped situation that prevents an effective plasmonic resonance.[25,30]

Here we propose and experimentally demonstrate all-PCM and lithography-free THz plasmonic metasurfaces based on laser printing of a thin film of In_3SbTe_2 (IST). IST is categorized as next-generation "plasmonic PCM" that undergoes a dielectric-to-metal phase transition upon crystallization,[31,32] providing a versatile platform for actively manipulating electromagnetic waves. Previous works have mainly focused on the infrared spectral range,[31–33] while the applications of IST at terahertz frequencies are still underexplored. In the following, we show the large difference in terahertz optical properties between the dielectric amorphous state (a-IST) and the metallic crystalline state (c-IST) in an ultra-broadband. By employing a nanosecond pulse laser to locally crystallize a thin film of a-IST, we are able to produce large-scale and ultrathin THz plasmonic metasurfaces with effective plasmonic resonances. We also show the first optical-pump terahertz-probe experiments on IST metasurfaces and demonstrate dynamic modulation of the transmission resonances, where photocarriers in both a-IST and c-IST regions together provide tunability of metasurfaces.

Y. Zeng, D. Lu, J. Wang, X. Yang, M. Xu, X. Zhang, P. Li
School of Optical and Electronic Information
Wuhan National Laboratory for Optoelectronics
Huazhong University of Science and Technology
Wuhan 430074, China
E-mail: xiaosheng_yang@outlook.com; lipn@hust.edu.cn

Y. Zeng, D. Lu, J. Wang, X. Yang, M. Xu, X. Zhang, P. Li
Optics Valley Laboratory
Hubei 430074, China

X. Xu, X. Zhang, H. Wan, Q. Wen, M. Hu
Terahertz Research Center
School of Electronic Science and Engineering
University of Electronic Science and Technology of China
Chengdu 610054, China
E-mail: hu_m@uestc.edu.cn

X. Xu, X. Zhang, H. Wan, Q. Wen, M. Hu
Key Laboratory of Terahertz Technology, Ministry of Education
Chengdu 610054, China

X. Jiang
Bruker (Beijing) Scientific Technology
Beijing 100081, China

J. Yao
School of Precision Instruments and Opto-Electronics Engineering
Tianjin University
Tianjin 300072, China

The ORCID identification number(s) for the author(s) of this article can be found under https://doi.org/10.1002/adom.202202651.

DOI: 10.1002/adom.202202651

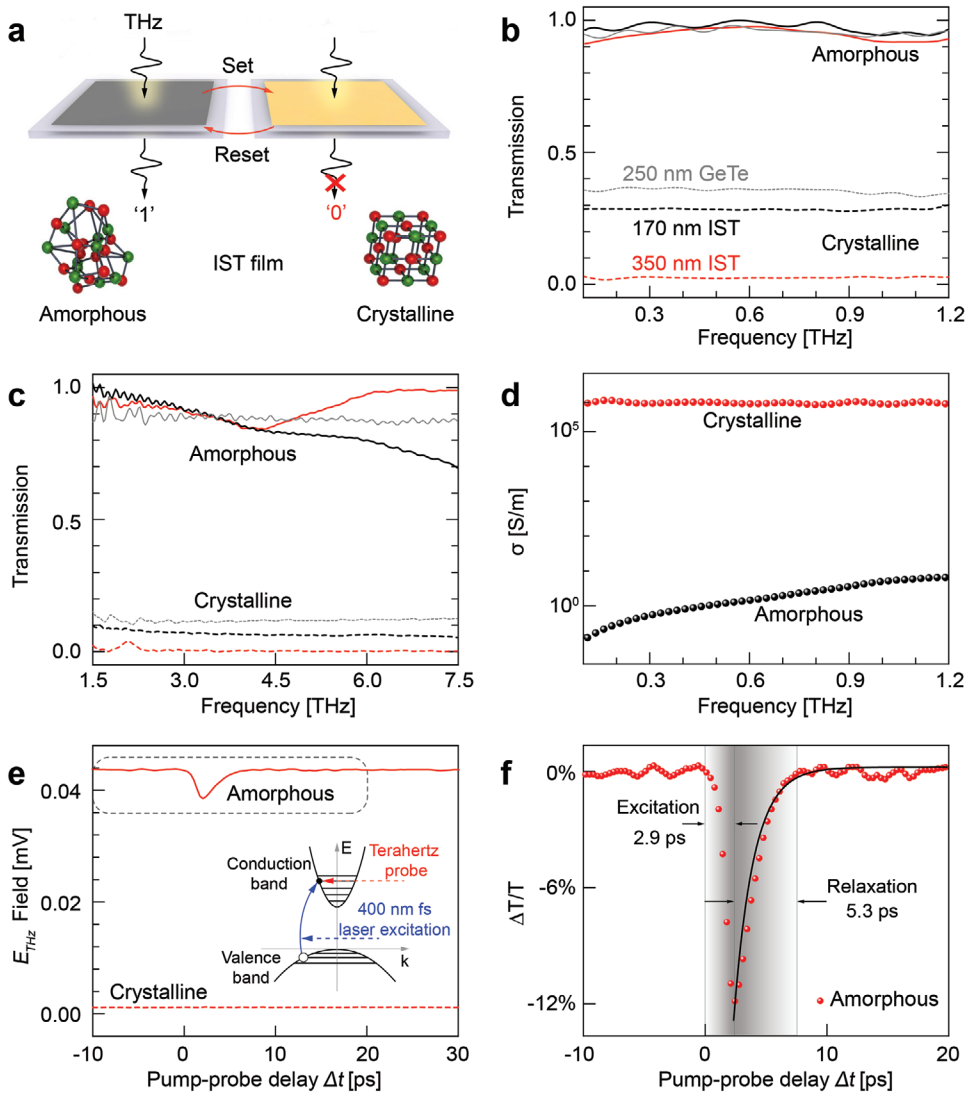

Figure 1. Terahertz transmission of IST films. a) Schematic of the IST film permitting or shielding the terahertz wave by changing between two crystallographic states. Normalized THz transmissions of IST and GeTe films in amorphous (solid line) and crystalline (dashed line) states with different thickness are measured by b) TDS and c) FTIR. d) Terahertz conductivity of the 350-nm IST film extracted from the data in (b). e) Pump-induced change of the terahertz peak electric field for the 350-nm IST film in amorphous and crystalline states as a function of the pump–probe delay time. f) Dynamic change of the terahertz transmission $\Delta T/T$ extracted from the dashed frame in (e), solid line indicates the fit result (see Experimental Section).

2. Results and Discussion

While THz optical properties of conventional PCMs (e.g., $Ge_2Sb_2Te_5$, $Ge_1Sb_2Te_4$, GeTe) are accessible in the literature,[34–36] we report the first THz transmission experiment of the emerging plasmonic PCM, IST. The IST film was deposited on a THz-transparent sapphire substrate, capped with a thin protection layer of SiO_2. The as-deposited film was initially in the state of a-IST. After annealing at 300 °C for 10 min, it was thermally switched to the crystalline phase[37] with resistivity reduction of more than six orders of magnitude and significant change in structure (Figure S1, Supporting Information). For obtaining ultra-broadband THz transmission spectra (0.3–7 THz), both IST states were measured with THz time-domain spectroscopy (TDS) and Fourier transform infrared spectroscopy (FTIR). Note that the spectra measured by the two methods may show discrepancies due to separate data normalization.

Figure 1b,c shows the measured broadband THz transmittance spectra of IST thin films (two different thicknesses: black lines, 170 nm; red lines, 350 nm). It can be seen that all spectra are rather flat as the frequency changes, without exhibiting obvious spectral features of THz phonon absorption (except a minimum of a-IST in Figure 1c due to the asymmetric Fabry–Perot cavity effect), in contrast to recent experiments of $Ge_1Sb_2Te_4$ (ref. [38]). For all measured frequencies, the 350-nm-thick a-IST film is almost transparent (transmittance $T > 0.9$), in remarkable contrast to its metallic c-IST counterpart that is highly reflective ($T < 0.05$). Such transmission contrast becomes weaker for the thinner IST (170 nm) due to the much higher transmission of the c-IST state. This is because the surface plasmons of plasmonic materials have limited scale

of energy concentration. In the case of c-IST, the skin depth is calculated to be ≈290 nm at 0.55 THz. But it is still obviously larger than that of a 250-nm-thick GeTe film (gray lines), illustrating the good performance of IST in screening the THz transmission. For a conductive film, the Fourier transforms of the time-dependent fields are related to the complex conductivity of the films via the thin film equation[39,40]

$$T(\omega)=\left|T(\omega)\right|e^{i\varphi(\omega)}=\frac{E(\omega)}{E_0(\omega)}=\frac{1+n_s}{1+n_s+Z_0 d\sigma(\omega)} \quad (1)$$

where E (E_0) is the extracted complex spectra of the Fourier transform of the terahertz wave forms through the sample with (without) the IST film, Z_0 is the vacuum impedance, d is the film thickness, and n_s is the refractive index of the substrate, φ is the phase, and $\sigma(\omega)$ is the complex conductivity of the film. The calculated permittivity and conductivity of dielectric a-IST are shown in Figure S2, Supporting Information. The c-IST film (350 nm, $\approx\lambda/2800$ when wavelength λ approximates to 1 mm at 0.3 THz) shows conductivity about five to seven orders of magnitude higher ($\approx 10^6$ S m^{-1}) than that of the a-IST film. $\omega_p = 7.3 \times 10^{15}$ Hz (Drude plasma frequency) and $\tau = 2$ fs (scattering time of free carriers) of c-IST were extracted by fitting the complex conductivity to the Drude–Smith model (Figure S3, Supporting Information). The results demonstrate that the c-IST film is akin to a metallic layer and possesses large optical and electrical contrast to its amorphous state. Overall, the switchable IST thin film shows excellent combined advantages of high efficiency and simplicity for tuning and modulating THz waves.

To characterize the response of THz ultrafast modulation with IST thin films, we performed ultrafast pump–probe transmission experiments. The 350-nm IST films were excited by 400-nm light pulses at 800 μJ cm^{-2} fluence (the highest available on our experimental setup to ensure that a-IST and c-IST are both in the excited states). We note that the photoexcitation time and the relaxation time of the THz modulation for IST are essentially independent of the pump fluence (Figures S4 and S5, Supporting Information), in line with recent report on the dynamics of charge carriers in GST films.[28] The employed photon energy (3.1 eV) is larger than the band gaps of both c-IST (0.45 eV) and a-IST (0.70 eV) according to calculations (Figure S6, Supporting Information). When optically pumped, the excited free charge carriers increase the film conductivity and decrease the terahertz transmission, before quickly decaying back to the equilibrium state.[28,41] However, Figure 1e shows that such charge carrier dynamics is only found for the a-IST film and there is no noticeable change in the transmitted terahertz field for the c-IST film. The latter is resulted by the highly delocalized electrons in c-IST, where the THz transmission is already so suppressed that contributions of pump-induced free carriers in transmission is not observable. Note that for clarifying the time dependence of c-IST, one could measure ultrafast transmission of ultrathin c-IST films or measure ultrafast reflectance of c-IST films. From the differential change ($\Delta T/T$) of THz transmission in Figure 1f, we determine that the excitation and recombination time of photo-generated carriers in the a-IST film are 2.9 and 5.3 ps, respectively, following the standard fitting procedure[42,43] (Experimental Section). The full width at half maxima (FWHM) of this curve is 2.3 ps. The observed dynamics of photo-generated charge carriers of a-IST is similar to other phase change materials such as GST[28] and GeTe[44] in terms of the excitation time, relaxation time, and maximum modulation depth.

Ultrafast responses of IST thin films hold great promise for THz devices with a high operational speed. On the other hand, the drastic difference in THz optical responses of a- and c-IST states prompts us to directly pattern c-IST "metallic" structures in the single a-IST thin film without the need of cumbersome lithography. To this end, we applied a nanosecond pulsed laser beam (power 70 mW, pulse duration 80 ns, see Experimental Section) to scan over a 350-nm a-IST film. Through laser-induced local thermal crystallization, we thus optically printed the arrays of c-IST split ring resonators (SRRs) in the a-IST film, as illustrated in **Figure 2**a. The inset of Figure 2a shows a photograph of a 2 × 2 cm^2 sample with four squares, each containing 5000–15 000 SRRs arranged in an array. The morphology of such device under the optical microscope is displayed in Figure 2b, with geometrical parameters annotated: periodicity (P), side length (L), and gap size (g). The morphology image showcases the homogeneously distributed microstructures and the clear edge between c-IST and a-IST, illustrating the high fabrication quality of direct laser writing of the metasurface structures.

To characterize polarization-controlled THz responses of the printed SRR metasurfaces, we measured their far-field transmittance for both transverse-electric (TE) and transverse-magnetic (TM) polarizations. In Figure 2c,d, we show the experimental spectra of two metasurface samples consisting of different-sized SRRs. For TE polarization, the sample A (P = 40 μm, L = 25 μm, g = 3 μm) shows three dips in the transmission spectrum (Figure 2c, solid red line, indicated by red arrows) at frequencies of 0.58, 1.80, and 2.52 THz, respectively. The simulated spectrum (Figure 2c, dashed red line) well reproduces these dips and confirms that they result from SRR resonance modes of the first three orders (TE1, TE2, and TE3). The mode profiles can be identified from the simulated electric-field intensity distributions shown in Figure 2e. For TM polarization, the sample A shows only a single transmission dip at f = 1.5 THz (see Figure 2d, red line). We assign this dip to the TM1 mode of the SRR, according to the simulated spectrum (dashed red line in Figure 2d) and the near-field distribution (Figure 2e). Those distinct resonant responses for TE and TM polarizations thus verify the functionality of IST metasurfaces for the polarization-control of THz waves.

For the sample B (P = 75 μm, L = 60 μm, g = 3 μm), we observed only a single transmission dip for each polarization (black lines in Figure 2c,d), respectively. These two dips correspond to TE2 and TM1 modes of the SRR, respectively, corroborated by simulations (dashed black lines, see also Figure S7, Supporting Information). Compared to the spectrum of the sample A, the spectral positions of the two resonant modes are drastically redshifted due to the larger periodicity and size of SRRs. Figure 2f further shows a contour plot displaying the simulated transmission of the SRR metasurface (sample A) as a function of the frequency and the polarization angle θ. We see that the spectral positions of the SRR resonances can be tuned by varying the angle θ. One can thus tune

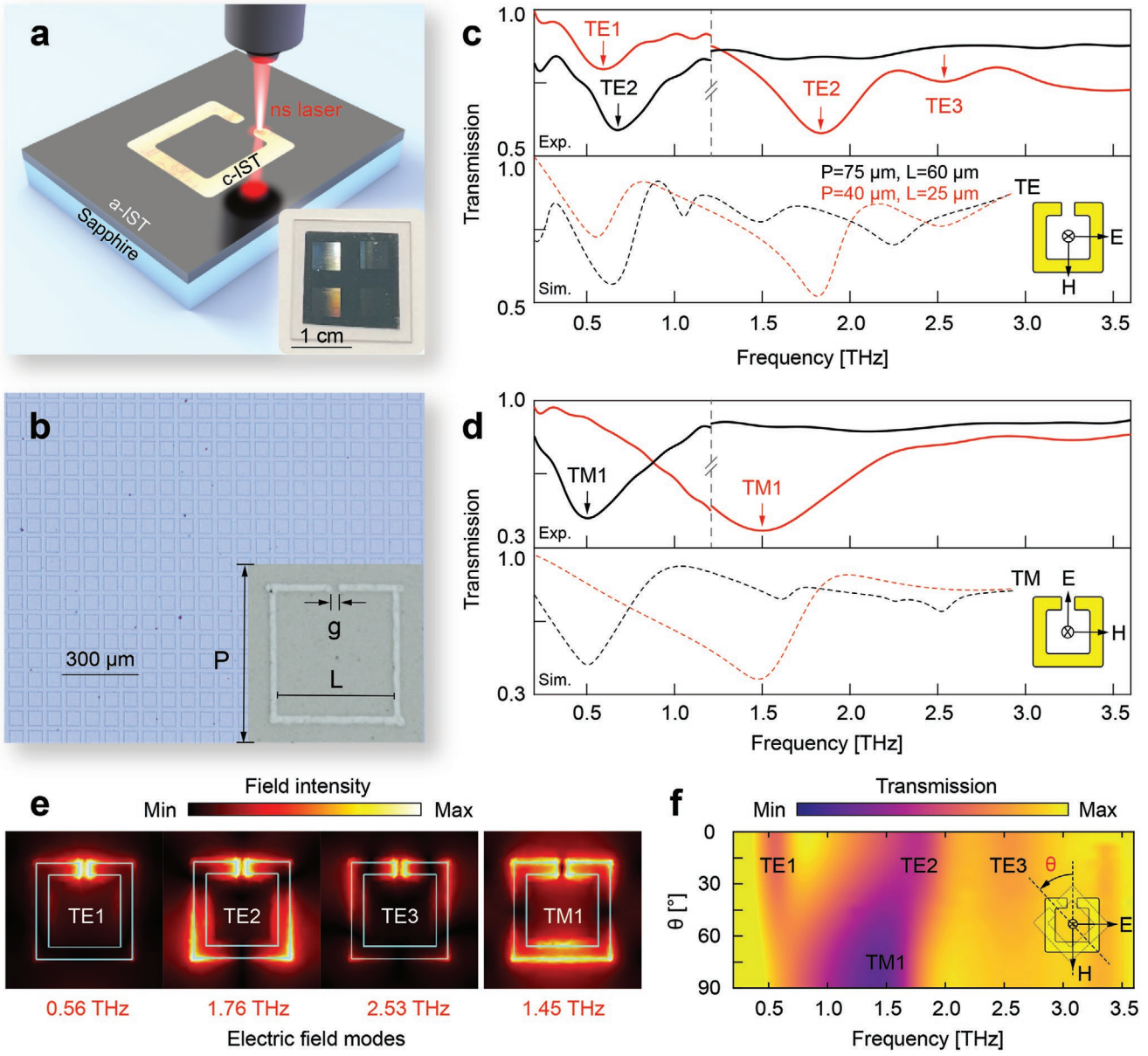

Figure 2. Terahertz resonance of the laser-printed IST metasurface. a) Schematic of printing a split ring resonator (SRR) in a 350-nm-thick a-IST film by scanning a pulsed laser beam with 70 mW power and 80 ns pulse duration. Inset: photograph of a 2×2 cm^2 sapphire chip with four regions containing SRR arrays. b) Optical microscope of a printed SRR array and geometrical parameters of its unit cell (inset): periodicity $P = 75$ μm, side length $L = 60$ μm, and gap size $g = 3$ μm. In this work, the gap (g) and the line width are fixed at 3 μm. c,d) Experimental and simulated terahertz transmission of two metasurfaces (sample A: $P = 40$ μm, $L = 25$ μm; sample B: $P = 75$ μm, $L = 60$ μm) with the electric field polarization of the incident wave parallel (TE) and perpendicular (TM) to the gap, respectively. e) Simulated electric field distribution of different excited modes (sample A). f) Simulated transmission of the SRR metasurface (sample A) as a function of the frequency and the polarization angle θ.

the resonances by changing different metasurface parameters, including the a- and c-IST states, the geometric sizes and the polarization angle.

Figure 2 demonstrates that IST metasurfaces exhibit polarization-dependent THz resonances of relatively narrow bandwidths, by comparing with IST films showing ultra-broadband THz optical contrasts (Figure 1). In which way IST can be utilized depends on different application purposes. For instance, the resonant near-field enhancement of the metasurfaces (Figure 2e) is suitable for promoting THz light-matter interaction. To measure the near-field responses of the IST metasurfaces, we combined scattering-type scanning near-field optical microscopy (s-SNOM) with a TDS system[45–47] for measuring near-field responses of printed IST metasurfaces. In such a system, the metallic atomic force microscope (AFM) tip of s-SNOM in the vicinity of the sample was illuminated by a linearly polarized, broadband THz pulse. Note that the oblique illumination has a large incident angle (~60°) with respect to the normal of the surface, which may distort the intrinsic field distribution of a photonic structure. The scattered signal from

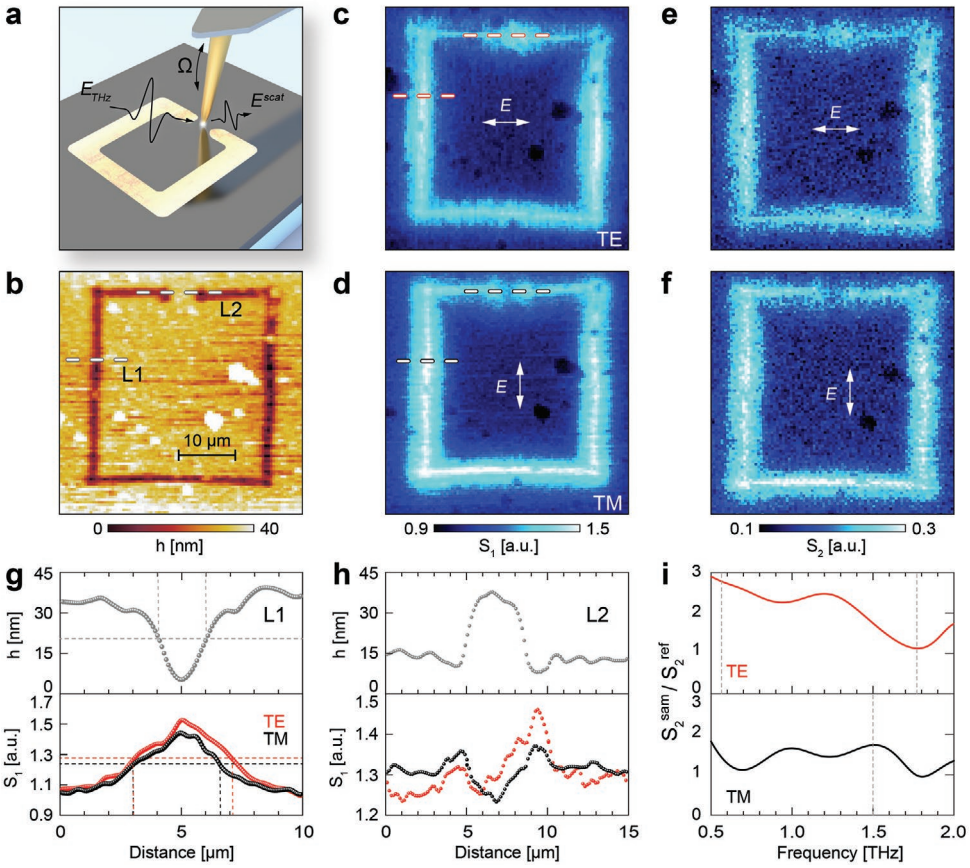

Figure 3. THz s-SNOM nano-imaging of the laser-printed IST metasurface. a) Schematic of real-space nano-imaging of the printed anisotropic metasurface measured by the s-SNOM with a TDS system. b) AFM topographic image of a printed SRR in the array of sample A. c,d) Near-field images SRR (amplitude signal S_1) of the same SRR for TE and TM modes. e,f) Near-field images SRR (amplitude signal S_2) of the same SRR for TE and TM modes. Signals S_1 and S_2 are normalized to the background intensity measured on the center a-IST of the images. g,h) Amplitude and near-field signal (S_1) profiles along the dashed lines L1 and L2 in (b–d). i) Normalized near-field signal spectra S_2^{gap}/S_2^{ref}, where S_2^{gap} and S_2^{ref} are the amplitude signal measured at the SRR's gap and the surrounding a-IST far away from the SRR array, respectively. Vertical dashed lines are resonance positions taken from Figure 2c,d as references.

the sample was then recombined with a controlled delay pulse onto the detector (illustrated in **Figure 3**a). At a fixed position of the s-SNOM tip over the sample, one can obtain single near-field THz-TDS spectra by sweeping the time delay Δt of the reference pulse.

To suppress the background, we obtained demodulated scattered signal S_n with a lock-in amplifier according to the nth harmonics of the tip tapping frequency Ω. The higher order signal contains less background. For measuring near-field images, we first adjusted the time delay to obtain the spectral integrated peak near-field THz-TDS signals on the center of the image (center a-IST in the SRR). By scanning and collecting near-field signals on each tip position over the metasurface sample, we obtained 2D near-field THz image with deeply subwavelength-scale THz optical resolution (determined by the radius of tip apex). By rotating the sample (with respect to the laser beam), we measured near images of the metasurfaces for TE and TM polarizations.

The sample topography image was simultaneously recorded during the scanning of AFM tip position (Figure 3b). Depressions can be found in the switched c-IST region compared to the neighboring a-IST area due to the increased density of crystalline phase.[48] We show THz near-field images in Figure 3c–f (TE and TM polarizations) for both S_1 and S_2 near-field signals. The higher harmonic S_2 signal has far-field background less than S_1 and typically shows the near-field image distinguished from that of S_1. Here the two signals observe the same near-field patterns, implying a negligible background. All these near-field images show that the c-IST SRR displays stronger signals than the surrounding a-IST due to the higher reflectivity. Further, the optical width of the SRR arm is remarkably wider than its geometric width measured from the topography, as shown by the AFM topography and optical profiles (Figure 3g). For the same position on the left arm, we see that the optical width (FWHM) of the SRR arm depends on polarization: 4.1 (TE) and 3.6 μm (TM). Both values are larger than the topography width of 2 μm. This observation can be explained by an inhomogeneous crystallization resulting from the Gaussian distribution of laser power[49] or by local optical fields extended from the resonators, or by the combination of both effects. Further in-depth THz-SNOM experiments and simulations will be helpful for clarifying it more clearly.

We further observe polarization dependences of the SRR in the near-field images. For TE (TM) polarization, the right (bottom) arm shows a larger optical signal than the left (upper) arm. Most importantly, we observe a remarkably asymmetric near-field distribution on the gap of the SRR for TE polarization (Figure 3c–e, red dots in Figure 3h), while for TM polarization the gap near-fields are more symmetric (Figure 3d–f, black dots in Figure 3h). According to recent THz-SNOM experiments,[50,51] such polarization-dependent asymmetric field distribution in the gap is typical for SRR resonant modes, which are intrinsically symmetric but distorted by the interference of oblique incidence in the s-SNOM setup. We also measured THz near-field spectra on the SRR gap, revealing multiple features of dips and peaks (Figure 3i, see also simulations in Figure S8, Supporting Information). Future studies using a monochromatic source (instead of the broadband source used in this work) and a sophisticated tip–sample coupling model of THz s-SNOM may help to verify and elucidate the near-field data.

For evaluating dynamic modulation properties, we executed far-field pump–probe experiments for the laser-printed IST metasurface (sample A). **Figure 4**a shows the differential transmission $\Delta T/T$ as a function of the pump–probe time delay Δt with various pump fluences. It is seen that the largest modulation (the dip in $\Delta T/T$) is reached at ≈1.8 ps after the pump excitation. The modulation strength increases from 4.1% (127 μJ cm^{-2} pump fluence) to 19.6% (762 μJ cm^{-2}) with rising pump fluence, while the FWHM of the dip in $\Delta T/T$ remains almost unchanged (1.6 ps) for different pump fluences, suggesting that an ultrafast and stable response time for modulation is facilitated by the IST metasurface. Table S1, Supporting Information, gives a literature survey on the terahertz ultrafast response of representative materials, which shows IST as a competitive alternative in terms of the response time and modulation depth.

By executing Fourier transform for the probe pulse (see Experimental Section), we obtained THz transmission of IST metasurfaces at various pump–probe delays Δt (pump fluence 635 μJ cm^{-2}). The results verify the dynamical modulation of the transmission resonances (see also the phase modulation in Figure S9, Supporting Information) of TE1, TE2, and TM1 modes (sample A, Figure 4b,c) and, more interestingly, further reveal the modes showing distinctive temporal variations. For instance, when strongly modulated (e.g., Δt = 1.4 ps), TE2 and TM1 modes show a clear red shift in their resonance frequencies (indicated by red arrows), while the frequency position of TE1 mode is slightly blue-shifted (blue arrow). To better compare such temporal differences, we traced the transmittance (values taken from the dips) of TE1, TE2, and TM1 modes for different time delay Δt (Figure 4d). As a reference, the results of a-IST film are also displayed in Figure 4d (purple symbols, see also Figure S4a, Supporting Information). Comparing those results, we see that the TE1 mode (red symbols) exhibits the temporal change showing a transmission dip at Δt = 1.8 ps. In contrast, the TM1 and TE2 modes show transmission peaks at Δt = 1.4 ps, the latter further showing a transmission dip at Δt = 1.8 ps. To quantitatively illustrate the dynamic coupling and damping mechanism, Figure 4e,f shows two sets of normalized fitting values, the resonance frequency ω, the damping rate γ and the coupling strength g for TE1 and TE2 modes, respectively, within the coupled Lorentz oscillator model as a function of Δt (cf. Figures S9 and S10, Supporting Information). The normalization was done by calculating the ratio of each parameter at dynamic and static conditions, respectively, minus unity, for example, $\omega_{\text{normalized}} = \omega_{\text{dynamic}}/\omega_{\text{static}} - 1$. Overall, γ and g undergo a similar change during the excitation and relaxation, namely first increasing and then decreasing with the delay time, in contrast to the much smaller change of ω. The parameters γ and g of TE1 has additionally a quick drop at 1.8 ps, possibly due to the different speed of excitation onset of a-IST and c-IST. The absence of such additional behavior for TE2 can be rationalized by its electric field that is more distributed on the ring and therefore less sensitive to the dynamic change of a-IST in the gap upon excitation (see the inset in Figure 4f). We highlight that such distinctive temporal responses result from the all-PCM nature of our printed IST metasurfaces, providing advantages of more functionalities over conventional metallic or PCM-incorporated metasurfaces.

In Figure 4g, we show that the resonances of the IST metasurface can also be tuned by adjusting the pump fluence. When increasing the pump fluence, the overall transmission is continuously decreased and the resonances are gradually suppressed. Our all-PCM metasurfaces exhibit ultrashort response time and bear the potential to enable reconfigurable THz photonics beyond the resonance modulation.

3. Conclusions

In conclusion, we have demonstrated a flexible platform of laser-printed THz metasurfaces made with ultrathin films of the plasmonic phase change material IST. Our findings highlight that the crystalline states of IST have Drude-like plasmonic behavior in the terahertz range and can be effectively utilized as an excitable metal in terahertz metasurfaces. We envision the IST-based, all-PCM photonic platform to be a complementary companion to conventional metallic meta-structures (see Figure S11, Supporting Information, for a comparison between IST-based SRR and noble-metal SRR) and other tunable plasmonic devices using, for example, graphene/insulator stacks,[39,52] providing a new degree of flexibility via optical control of PCM's bonding nature. We remark that the reversible crystalline-to-amorphous switching of IST infrared photonic devices has been demonstrated[31–33] (cf. Figure S12, Supporting Information). Compared to those infrared devices, THz devices require a larger size of patterned structure and thus enlarged volume that needs to be switched by laser. For amorphization of IST, short laser pulses with high power are needed, leading to the laser beam size smaller than the geometric sizes of our laser-written THz elements. Thus, it is time-consuming and not efficient to completely "erase" the arrays of THz elements. With progress in laser alignment and optimized thermal design, an extension to re-amorphization of IST for reversible switching is feasible. A combination with volatile switching based on electric biasing or thermal heating may enrich further possibilities for dynamic THz modulation.

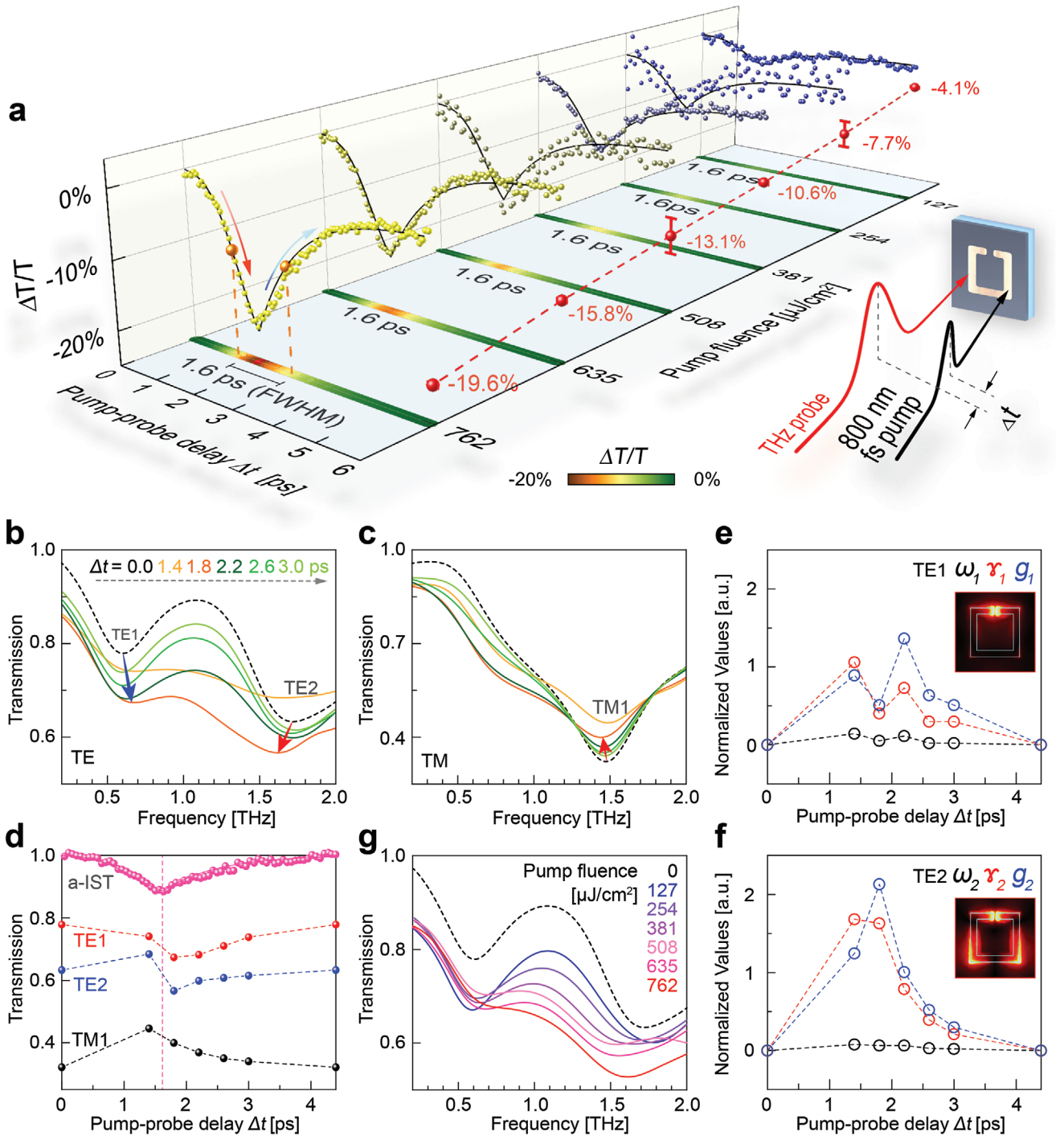

Figure 4. Picosecond evolution of volatile terahertz wave manipulation of the printed IST metasurface. a) Relative pump-induced change to the transmission ($\Delta T/T$) of metasurface as a function of the pump fluence and the pump–probe delay time Δt. Error bars are deviations calculated from fits and experimental data at the peaks. Solid line indicates the fit result (see Experimental Section). Inset: Schematic of the ultrafast optical-pump terahertz-probe experiment on the IST metasurface. b,c) Time evolution of the ultrafast terahertz resonance modulation (TE and TM modes) at 635-μJ cm^{-2} pump fluence. d) Transmission change of resonance dips for TE1, TE2, and TM1 modes as a function of Δt at 635-μJ cm^{-2} pump fluence. The total transmission change obtained on an a-IST film is shown as a reference. e,f) Normalized resonance frequency ω, damping rate γ and coupling strength g for TE1 and TE2 modes, respectively, by fitting the experimental curves in b) within the coupled Lorentz oscillator model. g) Transmission change as a function of the pump fluence at Δt = 1.8 ps corresponding to the time of peak positions in (a).

4. Experimental Section

Sample Fabrication: In_3SbTe_2 (IST) was deposited on 400-μm-thick sapphire substrates using stoichiometric targets by direct current magnetron sputtering (2×10^{-6} mbar background pressure, 20 s.c.c.m. Ar flow, 0.15 nm s^{-1} deposition rate). The thickness of IST film was controlled by a stylus profiler (Brucker DektakXT). Subsequently, 80-nm-thick SiO_2 was deposited on top of the IST film as a protective

capping layer by radio frequency magnetron sputtering. The as-deposited IST films were in the amorphous state, the crystalline state of IST shown in Figure 1 was achieved by heating in a vacuum oven at 300 °C for 10 min.

Laser Printing: A customized setup was built for patterning the IST film by focusing a laser beam through a ×20 objective (numerical aperture = 0.4) on the sample surface. A nanosecond laser diode source with a central wavelength of 660 nm provides single pulses with tunable output power (up to 400 mW) and pulse duration (from 1 ns to 10 µs). To crystallize the IST film, laser pulses of 70 mW power and 80 ns duration were used. An x–y movable sample stage with maximum range of 50 mm in each direction and minimal step size of 700 nm was used to prepare the structures shown in Figures

2–4. The repetition rate of the setup can be tuned between 1 Hz and 10 MHz, with scanning speed up to 20 mm s^{-1}. In the laser writing, the scanning speed was set at 4–8 mm s^{-1}, while the corresponding repetition rate was not less than 20 kHz.

Broadband Terahertz Spectrum Measurement: A Bruker Vertex 80v Fourier transform infrared (FTIR) spectrometer was used to measure the high frequency terahertz transmission spectrum of the IST film with a resolution of 0.03 THz from 1.5 to 7.5 THz.

Terahertz Time-Domain Spectroscopy: In order to observe the higher order modes of the metasurface, two THz sources were used. One was generated by exciting a photoconductive semiconductor InAs antenna with a 1560- nm femtosecond laser (Menlo Systems GmbH, Germany) and another was generated by exciting a $LiNbO_3$ waveguide with a 1560-nm femtosecond laser (Advantest, Japan). A photoconductive antenna was used for detecting the transmitted THz pulses. The whole beam path was purged with dry nitrogen gas, which results in higher signal-to-noise ratio due to the moisture removal (same with the near-field and pump-probe beam path described below).

THz Scattering-Type Scanning Near-Field Optical Microscopy: The measurements were performed with an s-SNOM (NeaSpec GmbH, Germany) and the THz radiation was generated by exciting a photoconductive antenna with a 1560-nm femtosecond laser (Menlo Systems GmbH, Germany). The atomic force microscopy (AFM) probe was 80 µm long (Rocky Mountain Nanotechnology LLC, USA), with the THz wave illuminating the tapping tip for signal modulation. The first and second order near-field signals (S_1 and S_2) were obtained by demodulating the tip-scattered signal at the first and second harmonic of the tip's oscillation frequency Ω to remove the background signal, as was routinely done in s-SNOM.

Ultrafast Optical-Pump Terahertz-Probe Spectroscopy: The setup was based on a ZnTe crystal which provides nonlinear terahertz generation (optical rectification) and detection (electro-optic sampling). A femtosecond laser (800 nm center wavelength, <50 fs pulse duration, 1 kHz repetition frequency) was divided into three beams: the generation and detection of terahertz pulses, and the photoexcitation of the IST sample. The 400-nm pump laser (3.10 eV) in Figure 1 used the second harmonic generated from a β-barium borate crystal. The 800-nm excitation light pulses were used in all pump–probe measurements since the photon energy (1.55 eV) is larger than the bandgap of IST (Figure S6, Supporting Information) for both phases, except that in Figure 1e,f the 400-nm pump laser (3.10 eV, second harmonic generated from a β-barium borate crystal) was used. This work noted that, for the a-IST film, the change of photon energy from 3.10 eV (400 nm) in Figure 1f to 1.55 eV (800 nm) in Figure 4d reduces the effective mass of charge carriers, leading to the shorter scattering time and thus the decreased FWHM of the THz transmission transient. For the pump–probe measurements, the pump delay stage between optical-pump and terahertz-probe pulses was scanned (Δt, in Figures 1e,f and 4a). For the spectral analysis of the pump-induced resonance changes (in Figure 4b,c,g), the pump time delay was set at fixed position for a specific Δt, while the THz delay time was varied to scan the transmitted terahertz pulse.

Fitting for Differential Transmission Data: The excitation and the recombination time of the a-IST film and the printed metasurface were extracted by fitting the data points to an error function $f(t) = a \times \mathrm{erf}(t-\tau_1) + b$ and an exponential decay function $f(t) = c \times \exp(-t/\tau_2) + d$, respectively, where τ_1 and τ_2 are time constants of the excitation and the recombination processes, and a, b, c, d are offset parameters.[42,43]

Numerical Simulation: The terahertz response of the printed metasurface and the electric field distributions were simulated using the commercial software CST Studio Suite. The TE and TM floquet mode ports were set as the excitation and the receiver. Periodic boundary conditions were set in four sides of the unit cell. The static terahertz dielectric and conductivity settings of IST were shown in Figures S2 and S3, Supporting Information. Variable polarization angles were set in the phi option in phase shift/scan angles of the boundary conditions.

Supporting Information

Supporting Information is available from the Wiley Online Library or from the author.

Acknowledgements

Y.Z. and D.L. contributed equally to this work. P.L. acknowledges the support from the National Natural Science Foundation of China (Grant No. 62075070), National Key Research and Development Program of China (Grant No. 2021YFA1201500), Hubei Provincial Natural Science Foundation of China (Grant No. 2022CFA053) and the Innovation Fund of WNLO. M.H. acknowledges the support by National Key Research and Development Program of China under Grant 2017YFA0701000 and Natural Science Foundation of China under Grant 61988102, 61921002 and 62071108. We also thank the Analytical and Testing Center of HUST for help with the measurements.

Conflict of Interest

The authors declare no conflict of interest.

Data Availability Statement

The data that support the findings of this study are available from the corresponding author upon reasonable request.

Keywords

metasurfaces, phase change materials, terahertz, ultrafast optics

Received: November 7, 2022
Revised: February 11, 2023
Published online:

[1] D. Mittleman, Ed., *Sensing with Terahertz Radiation*, Vol. *85*, Springer, Berlin, Heidelberg, **2003**.
[2] M. Tonouchi, *Nat. Photonics* **2007**, *1*, 97.
[3] T. Nagatsuma, G. Ducournau, C. C. Renaud, *Nat. Photonics* **2016**, *10*, 371.
[4] T. J. Yen, W. J. Padilla, N. Fang, D. C. Vier, D. R. Smith, J. B. Pendry, D. N. Basov, X. Zhang, *Science* **2004**, *303*, 1494.
[5] D. R. Smith, J. B. Pendry, M. C. K. Wiltshire, *Science* **2004**, *305*, 788.

[6] H.-T. Chen, W. J. Padilla, J. M. O. Zide, A. C. Gossard, A. J. Taylor, R. D. Averitt, *Nature* **2006**, *444*, 597.
[7] W. Withayachumnankul, D. Abbott, *IEEE Photonics J.* **2009**, *1*, 99.
[8] I. B. Vendik, O. G. Vendik, M. A. Odit, D. V. Kholodnyak, S. P. Zubko, M. F. Sitnikova, P. A. Turalchuk, K. N. Zemlyakov, I. V. Munina, D. S. Kozlov, V. M. Turgaliev, A. B. Ustinov, Y. Park, J. Kihm, C-W. Lee, *IEEE Trans Terahertz Sci. Technol.* **2012**, *2*, 538.
[9] Q. Wang, E. Plum, Q. Yang, X. Zhang, Q. Xu, Y. Xu, J. Han, W. Zhang, *Light Sci. Appl.* **2018**, *7*, 25.
[10] L. Cong, Y. K. Srivastava, H. Zhang, X. Zhang, J. Han, R. Singh, *Light Sci. Appl.* **2018**, *7*, 28.
[11] X. Zang, B. Yao, L. Chen, J. Xie, X. Guo, A. V. Balakin, A. P. Shkurinov, S. Zhuang, *Light Adv. Manuf.* **2021**, *2*, 148.
[12] N. Raeis-Hosseini, J. Rho, *Materials* **2017**, *10*, 1046.
[13] M. Wuttig, H. Bhaskaran, T. Taubner, *Nat. Photonics* **2017**, *11*, 465.
[14] S. M. Choudhury, D. Wang, K. Chaudhuri, C. DeVault, A. V. Kildishev, A. Boltasseva, V. M. Shalaev, *Nanophotonics* **2018**, *7*, 959.
[15] F. Ding, Y. Yang, S. I. Bozhevolnyi, *Adv. Opt. Mater.* **2019**, *7*, 1801709.
[16] N. El-Hinnawy, P. Borodulin, B. P. Wagner, M. R. King, E. B. Jones, R. S. Howell, M. J. Lee, R. M. Young, *Appl. Phys. Lett.* **2014**, *105*, 013501.
[17] Y. Zhang, C. Fowler, J. Liang, B. Azhar, M. Y. Shalaginov, S. Deckoff-Jones, S. An, J. B. Chou, C. M. Roberts, V. Liberman, M. Kang, C. Ríos, K. A. Richardson, C. Rivero-Baleine, T. Gu, H. Zhang, J. Hu, *Nat. Nanotechnol.* **2021**, *16*, 661.
[18] Y. Wang, P. Landreman, D. Schoen, K. Okabe, A. Marshall, U. Celano, H.-S. P. Wong, J. Park, M. L. Brongersma, *Nat. Nanotechnol.* **2021**, *16*, 667.
[19] Q. Wang, E. T. F. Rogers, B. Gholipour, C.-M. Wang, G. Yuan, J. Teng, N. I. Zheludev, *Nat. Photonics* **2016**, *10*, 60.
[20] P. Li, X. Yang, T. W. W. Maß, J. Hanss, M. Lewin, A.-K. U. Michel, M. Wuttig, T. Taubner, *Nat. Mater.* **2016**, *15*, 870.
[21] K. Dong, S. Hong, Y. Deng, H. Ma, J. Li, X. Wang, J. Yeo, L. Wang, S. Lou, K. B. Tom, K. Liu, Z. You, Y. Wei, C. P. Grigoropoulos, J. Yao, J. Wu, *Adv. Mater.* **2018**, *30*, 1703878.
[22] M. Seo, J. Kyoung, H. Park, S. Koo, H. Kim, H. Bernien, B. J. Kim, J. H. Choe, Y. H. Ahn, H.-T. Kim, N. Park, Q.-H. Park, K. Ahn, D. Kim, *Nano Lett.* **2010**, *10*, 2064.
[23] Z. L. Sámson, K. F. MacDonald, F. De Angelis, B. Gholipour, K. Knight, C. C. Huang, E. Di Fabrizio, D. W. Hewak, N. I. Zheludev, *Appl. Phys. Lett.* **2010**, *96*, 143105.
[24] A. H. Gwin, C. H. Kodama, T. V. Laurvick, R. A. Coutu, P. F. Taday, *Appl. Phys. Lett.* **2015**, *107*, 031904.
[25] C. H. Kodama, R. A. Coutu, *Appl. Phys. Lett.* **2016**, *108*, 231901.
[26] C. Han, E. P. J. Parrott, G. Humbert, A. Crunteanu, E. Pickwell-MacPherson, *Sci. Rep.* **2017**, *7*, 12725.
[27] S. Wang, L. Kang, D. H. Werner, *Sci. Rep.* **2018**, *8*, 189.
[28] P. Pitchappa, A. Kumar, S. Prakash, H. Jani, T. Venkatesan, R. Singh, *Adv. Mater.* **2019**, *31*, 1808157.
[29] M. Pinaud, G. Humbert, S. Engelbrecht, L. Merlat, B. M. Fischer, A. Crunteanu, *ACS Photonics* **2021**, *8*, 3272.
[30] Q.-W. Lin, H. Wong, L. Huitema, A. Crunteanu, *Adv. Opt. Mater.* **2022**, *10*, 2101699.
[31] A. Heßler, S. Wahl, T. Leuteritz, A. Antonopoulos, C. Stergianou, C.-F. Schön, L. Naumann, N. Eicker, M. Lewin, T. W. W. Maß, M. Wuttig, S. Linden, T. Taubner, *Nat. Commun.* **2021**, *12*, 924.
[32] A. Heßler, L. Conrads, K. G. Wirth, M. Wuttig, T. Taubner, *ACS Photonics* **2022**, *9*, 1821.
[33] A. Heßler, S. Wahl, P. T. Kristensen, M. Wuttig, K. Busch, T. Taubner, *Nanophotonics* **2022**, *11*, 3871.
[34] F. Kadlec, C. Kadlec, P. Kužel, *Solid State Commun.* **2012**, *152*, 852.
[35] C. Chen, P. Jost, H. Volker, M. Kaminski, M. Wirtssohn, U. Engelmann, K. Krüger, F. Schlich, C. Schlockermann, R. P. S. M. Lobo, M. Wuttig, *Phys. Rev. B* **2017**, *95*, 094111.
[36] K. Makino, K. Kato, Y. Saito, P. Fons, A. V. Kolobov, J. Tominaga, T. Nakano, M. Nakajima, *J. Mater. Chem. C* **2019**, *7*, 8209.
[37] N. Saxena, C. Persch, M. Wuttig, A. Manivannan, *Sci. Rep.* **2019**, *9*, 19251.
[38] C. Chen, S. Chen, R. P. S. M. Lobo, C. Maciel-Escudero, M. Lewin, T. Taubner, W. Xiong, M. Xu, X. Zhang, X. Miao, P. Li, R. Hillenbrand, *ACS Photonics* **2020**, *7*, 3499.
[39] H. Yan, X. Li, B. Chandra, G. Tulevski, Y. Wu, M. Freitag, W. Zhu, P. Avouris, F. Xia, *Nat. Nanotechnol.* **2012**, *7*, 330.
[40] J. Lloyd-Hughes, T.-I. Jeon, *J. Infrared Millim. Terahertz Waves* **2012**, *33*, 871.
[41] Z. Jin, Y. Peng, Y. Fang, Z. Ye, Z. Fan, Z. Liu, X. Bao, H. Gao, W. Ren, J. Wu, G. Ma, Q. Chen, C. Zhang, A. V. Balakin, A. P. Shkurinov, Y. Zhu, S. Zhuang, *Light Sci. Appl.* **2022**, *11*, 209.
[42] S. Wall, D. Wegkamp, L. Foglia, K. Appavoo, J. Nag, R. F. Haglund, J. Stähler, M. Wolf, *Nat. Commun.* **2012**, *3*, 721.
[43] S. Kovalev, H. A. Hafez, K.-J. Tielrooij, J.-C. Deinert, I. Ilyakov, N. Awari, D. Alcaraz, K. Soundarapandian, D. Saleta, S. Germanskiy, M. Chen, M. Bawatna, B. Green, F. H. L. Koppens, M. Mittendorff, M. Bonn, M. Gensch, D. Turchinovich, *Sci. Adv.* **2021**, *7*, eabf9809.
[44] Y. Zeng, J. Wang, X. Yang, J. Yao, P. Li, Q. He, M. Xu, X. Miao, *Opt. Mater.* **2023**, *136*, 113447.
[45] J. Zhang, X. Chen, S. Mills, T. Ciavatti, Z. Yao, R. Mescall, H. Hu, V. Semenenko, Z. Fei, H. Li, V. Perebeinos, H. Tao, Q. Dai, X. Du, M. Liu, *ACS Photonics* **2018**, *5*, 2645.
[46] N. A. Aghamiri, F. Huth, A. J. Huber, A. Fali, R. Hillenbrand, Y. Abate, *Opt. Express* **2019**, *27*, 24231.
[47] X. Chen, X. Liu, X. Guo, S. Chen, H. Hu, E. Nikulina, X. Ye, Z. Yao, H. A. Bechtel, M. C. Martin, G. L. Carr, Q. Dai, S. Zhuang, Q. Hu, Y. Zhu, R. Hillenbrand, M. Liu, G. You, *ACS Photonics* **2020**, *7*, 687.
[48] W. K. Njoroge, H.-W. Wöltgens, M. Wuttig, *J. Vac. Sci. Technol., A* **2002**, *20*, 230.
[49] A. U. Michel, A. Heßler, S. Meyer, J. Pries, Y. Yu, T. Kalix, M. Lewin, J. Hanss, A. De Rose, T. W. W. Maß, M. Wuttig, D. N. Chigrin, T. Taubner, *Adv. Mater.* **2019**, *31*, 1901033.
[50] N. Sulollari, J. Keeley, S. Park, P. Rubino, A. D. Burnett, L. Li, M. C. Rosamond, E. H. Linfield, A. G. Davies, J. E. Cunningham, P. Dean, *APL Photonics* **2021**, *6*, 066104.
[51] L. Thomas, T. Hannotte, C. N. Santos, B. Walter, M. Lavancier, S. Eliet, M. Faucher, J.-F. Lampin, R. Peretti, *ACS Appl. Mater. Interfaces* **2022**, *14*, 32608.
[52] Y. Li, K. Tantiwanichapan, A. K. Swan, R. Paiella, *Nanophotonics* **2020**, *9*, 1901.